Seasonal Changes of Mélange Thickness Coincide With Greenland Calving Dynamics

Yue Meng (olivmeng@stanford.edu)
Stanford University https://orcid.org/0000-0001-7623-2228
Ching-Yao Lai
Stanford University
Riley Culberg
Cornell University
Michael Shahin
University of Kansas
Leigh Stearns
The University of Kansas https://orcid.org/0000-0001-7358-7015
Justin Burton
Emory University https://orcid.org/0000-0002-4797-8968
Kavinda Nissanka
Emory University

Article

Keywords:

Posted Date: January 25th, 2024

DOI: https://doi.org/10.21203/rs.3.rs-3893234/v1

Additional Declarations: There is **NO** Competing Interest.

Seasonal Changes of Mélange Thickness Coincide With Greenland Calving Dynamics

Yue Meng[1*], Ching-Yao Lai[1], Riley Culberg[2], Michael G. Shahin[3], Leigh A. Stearns[3], Justin C. Burton[4], and Kavinda Nissanka[4]

[1]Department of Geophysics, Stanford University, Stanford, CA, USA
[2]Department of Earth and Atmospheric Sciences, Cornell University, Ithaca, NY, USA
[3]Department of Geology, The University of Kansas, Lawrence, KS, USA
[4]Department of Physics, Emory University, Atlanta, GA, USA

January 24, 2024

* Corresponding author: olivmeng@stanford.edu

Abstract

Iceberg calving is a major contributor to Greenland's ice mass loss. Ice mélange, tightly packed sea ice and icebergs, has been hypothesized to buttress the calving fronts. However, quantifying the mélange buttressing force from field observations remains a challenge. Here we show that such quantification can be achieved with a single field measurement: thickness of mélange at the glacier terminus. We develop the first three-dimensional discrete element model of mélange along with a simple analytical model to quantify the mélange buttressing using mélange thickness data from ArcticDEM over 32 Greenland glacier termini. We observed a strong seasonality in mélange thickness: thin mélange (averaged thickness 34^{+17}_{-15} m) in summertime when terminus retreats, and thick mélange (averaged thickness 119^{+31}_{-37} m) in wintertime when terminus advances. The observed seasonal changes of mélange thickness strongly coincide with observed Greenland calving dynamics and the modeled buttressing effects.

The Greenland Ice Sheet (GrIS), holding 7.2 m of sea level equivalent, has become the largest single source of barystatic sea-level rise in the cryosphere [1, 2]. Under high carbon emission scenario, the GrIS is projected to contribute about 79–167 mm of sea-level rise by 2100, 30% to 60% of which comes from iceberg calving at marine-terminating glaciers [3, 4]. Projections of sea level rise by 2100 can vary by 400 mm depending on the rate of iceberg calving at ice sheet margins [5]. Calving laws used in current ice-sheet models predict calving rates using empirically tuned strain rate or stress criteria, which is inadequate to capture the complex external interactions that modulate calving and are strongly coupled with the warming climate [3, 6, 7, 8]. In particular, how calving depends on ice-ocean interactions is poorly understood.

Recent large calving retreats at some Greenland outlet glaciers have been correlated with rapid breakup of mélange, a collection of sea ice and icebergs tightly packed in tidewater glacier fjords adjacent to glacier termini [9, 10, 11, 12, 13, 14, 15]. Seasonal advance and retreat of glacier termini coincides with variations in mélange rigidity, which is affected by sea ice that grows in winter and decays in summer [16, 17, 18, 19, 20, 21]. These observations suggest that the presence of rigid mélange can mitigate iceberg calving by buttressing the glacier terminus. [22, 23, 24, 25, 17, 19, 26, 18, 27, 28, 29]. The force exerted by the mélange to support the glacier terminus is called the mélange buttressing force [28]. Prescribing a periodic change in the magnitude of the mélange buttressing force in ice-sheet models successfully reproduces observed seasonal calving dynamics [30, 31, 32, 25, 26, 33, 34, 4]. In a warming climate, a complete loss of mélange buttressing may prevent terminus advances in winter while exacerbating summer retreats, resulting in rapid glacier terminus retreats [4].

To capture physical processes that dictate the buttressing force magnitude, recent studies have taken a granular mechanics approach to quantify the flow and stress within ice mélange [27, 28]. Discrete element models [27] successfully reproduce the observed jamming wave propagation during calving events [35]. These experiments and discrete element models are two dimensional and assume a constant thickness of ice mélange and disk-shaped grains for simplicity. However, field observations show that mélange thickness can be non-uniform and decays with distance from the terminus [29, 23]. In early summer 2016 for Jakobshavn Isbræ, an unusually thick mélange wedge at the glacier front coincided with a one-month terminus quiescence period [23]. Continuum theories state that assuming mélange of a constant thickness, the mélange buttressing force per unit width linearly scales with mélange thickness ($F/W \sim H$) [28], whereas in three dimensions with along-flow mélange thickness variations, it scales with the square of the mélange thickness ($F/W \sim H^2$) built up at the terminus [29]. Therefore, it is crucial to consider the three-dimensional nature of mélange. To quantify the mélange buttressing force, previous two-dimensional models assuming mélange of uniform thickness require estimates of many parameters, including fjord/mélange friction/cohesion properties, and the mélange width/length [28]. Here we develop the first three-dimensional discrete element model to show that mélange thickness at the terminus is the only field measurement needed to estimate the buttressing force. We incorporate ICESat-2 and ArcticDEM observations to show that mélange thickness seasonality strongly correlates with calving dynamics of 32 Greenland tidewater glaciers.

1 Results

1.1 Mélange thickness associated with calving dynamics at Helheim Glacier in 2019-2020.

Throughout 2019, a REIGL VZ-6000 terrestrial laser scanner (TLS) scanned the terminus and ice mélange of Helheim Glacier, every 24 hours in the winter months, and every 6 hours in non-winter months (Fig. 1(a)). From the TLS point-cloud, we compute mélange surface elevation after accounting for local differences between the ellipsoid and geoid with tidal corrections [36]. Fig. 1(a) shows the resultant surface elevation field for ice mélange on 30 Nov 2019. To display the spatial profile of the mélange elevation, we calculate distances from terminus for all data points in the ice mélange and plot them as density maps in Fig. 1(c)-(f). For any specific distance from the terminus, there exists a spread of mélange elevation. We find the elevation value that has the maximum number of data points, and connect these elevation values along the distance from terminus as the representative mélange elevation profiles (solid blue lines in Fig. 1(c)-(f)). We exclude large icebergs which usually have elevation values larger than 30 m (Fig. 1(a)). To estimate mélange elevation near the glacier terminus (Z_0), we take an average of all data points within 1 km of the terminus. We infer thickness of the mélange based on TLS-derived surface elevations and assuming hydrostatic equilibrium.

To investigate the correlation between the mélange thickness and calving dynamics, we derive time series of mélange elevation at the terminus, calving events, and terminus position inferred from TLS data and satellite images (Sentinel-1, Sentinel-2 and Landsat 8) from 1 Sep 2019 to 1 Sep 2020 (Fig. 1(b)). With reference to previous classification of calving events [23], here, we define major calving events as those that cause significant iceberg motions within the mélange and an overall terminus retreat; minor calving events are those in which visible blocks calved, but the mélange or terminus position remained largely unchanged. We observe two time periods of terminus quiescence, from 8 Oct 2019 - 31 Dec 2019 and 1 Mar 2020 - 20 May 2020, when no calving occurred and the terminus advanced steadily. We found that mélange elevation at the terminus averaged 15 m during these periods. We identified four dates where noticeable mélange thinning occurred, which were 4 Sep 2019, 3 Jan 2020 (Fig. 1(d)), 31 May 2020 (Fig. 1(f)), and 18 July 2020. Around these four dates, the mélange elevation at the terminus decreased to 10.8$\pm$0.10 m, 10$\pm$0.10 m, 9.4$\pm$0.10 m, and 11.6$\pm$0.10 m, respectively. Major calving happened around these dates, with linear retreats at the terminus of 0.5 km, 1.2 km, 1.3 km, and 1.0 km, respectively. Comparisons of time-varying mélange thickness and calving dynamics at Helheim Glacier (Fig. 1(b) support the view that the buttressing force increases with the mélange thickness; it is also possible that the mélange thickness and the terminus may be reacting simultaneously but independently to other oceanic and atmospheric forcing, or that calving dynamics drive variations in mélange thickness instead of the other way around. To derive a completely unambiguous explanation, we would need in-situ observations with high temporal resolution in minutes to capture the sequence of a calving event and a mélange thinning event [14, 23].

1.2 Seasonal changes of mélange thickness and calving dynamics.

Remote sensing observations on many Greenland glacier termini have shown significant terminus-position seasonality, with advance in winter and retreat in spring to summer through enhanced calving [37, 38, 39]. Previous studies have attributed seasonal calving dynamics to buttressing from ice mélange [18, 15, 40]. To investigate whether there are correlations between ice mélange thickness and calving dynamics on other glaciers, we use ICESat-2 observations of mélange surface elevation. While this dataset does not provide the temporal resolution to study individual calving events, we can leverage the observed seasonality in terminus advance and retreat at many Greenland glaciers to assess whether mélange thickness is correlated with periods of quiescence versus vigorous calving.

We identify ICESat-2 tracks passing over glacier termini in different seasons for Jakobshavn Isbræ (Fig. 2(a)), Kangerlussuaq Glacier (Fig. 2(b)), and Store Glacier (Fig. 2(c)). Surface elevation data is acquired along the ICESat-2 track and displayed as a function of the distance from terminus. We compare the mélange surface elevation profile during two seasons for Jakobshavn Isbræ and Kangerlussuaq Glacier (Fig. 2(d)(e)): winter to early spring (solid black lines) and summer (dashed black lines). Near the termini, mélange for the two glaciers both exhibit distinctly different freeboard heights during the two seasons: $20 \sim 35$ m in winter, and below 5 m in summer. The seasonal changes in mélange thickness at the terminus may explain the observed calving dynamics and terminus motion: zero or minor calving with an advancing terminus from winter to spring, and vigorous calving with a retreating terminus from summer to fall (Fig. 2(g)(h)). At Store Glacier in 2019, the mélange was present from 1 Jan to 14 June, after which calving resumed and the terminus kept retreating (Fig. 2(i)). The mélange elevation profile on 22 March 2019 exhibits a thickness gradient with a freeboard height of around 30 m near the terminus (Fig. 2(f)). In summary, the available data supports the hypothesis that thick mélange in winter inhibits calving and leads to the seasonal terminus advance.

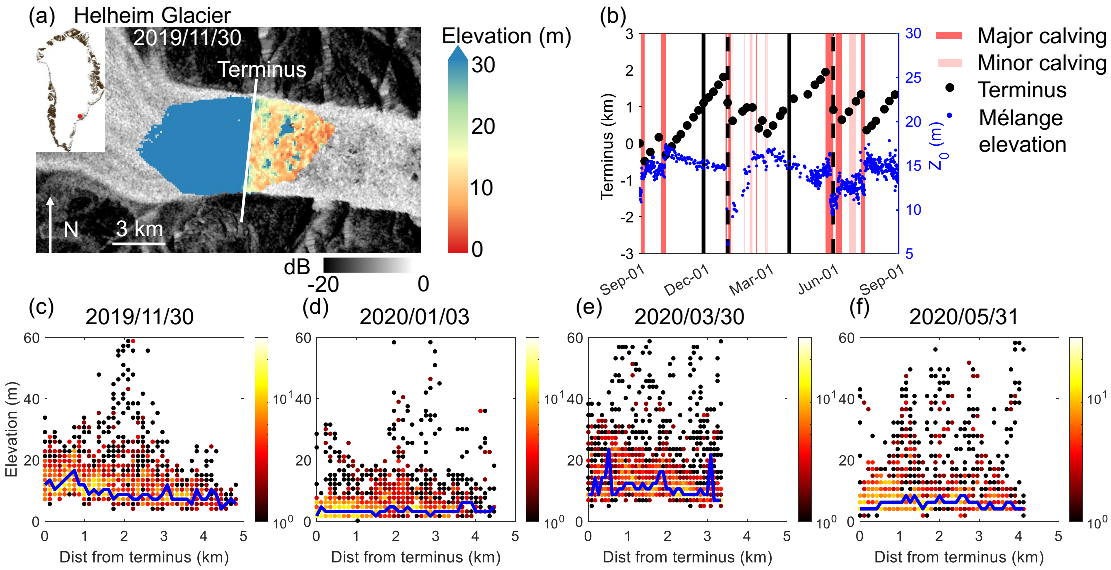

Figure 1: Helheim Glacier and ice mélange. (a) TLS-measured elevation map after accounting for local differences between the ellipsoid and geoid, overlain on a Sentinel-1 HV image (both acquired on 30 Nov 2019). The white line across the fjord indicates the glacier front location. The upper left inset shows the location of Helheim Glacier in Greenland. The image is in polar stereographic projection (EPSG: 3413). (b) Terminus position relative to 1 Sep 2019, where the positive sign indicates terminus advance. Blue dots denote the averaged mélange elevation within 1 km of the terminus, Z_0. Calving events are inferred from TLS and satellite images. Due to limited temporal sampling of the data, we are not able to determine the exact time of each calving event. Instead, we mark the time period during which a calving event occurs by a red-shade rectangle. Four vertical black lines mark the dates for the TLS-measured elevation data presented in (c)-(f), which corresponds to 30 Nov 2019, 3 Jan 2020, 30 Mar 2020, and 31 May 2020, respectively. Solid black lines mark the dates with terminus advances, and dashed black lines mark the dates with terminus retreats. (c)-(f) Surface elevation profiles for the mélange displayed as density plots (1510∼1859 data points in total); the colour bar denotes the number of data points that have the same elevation and distance from terminus values. For any specific distance from terminus, we find the elevation value that has the maximum number of data points. Solid blue lines connect these elevation values along the distance from terminus as the representative mélange elevation profiles. Mélange thinning on 3 Jan (d) and 31 May (f) coincided with more calving activities and terminus retreats as shown in (b).

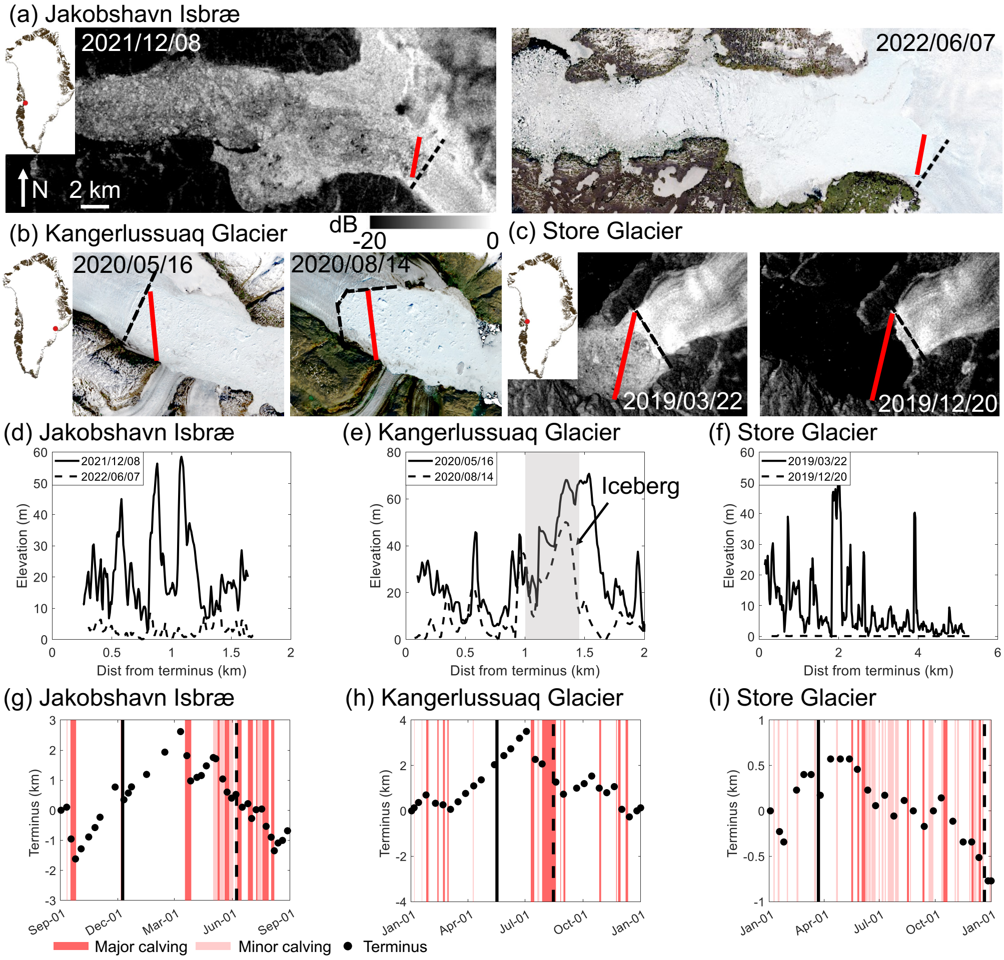

Figure 2: Seasonal changes of mélange thickness are correlated with calving dynamics and terminus position. (a) Sentinel-1 HV and Landsat 8 images for Jakobshavn Isbræ on 8 Dec 2021, 7 Jun 2022, respectively. (b) Landsat 8 images for Kangerlussuaq Glacier on 19 May 2020, 14 Aug 2020, respectively. (c) Sentinel-1 HV images for Store Glacier on 22 Mar 2019, 19 Dec 2019, respectively. In (a)-(c), the black dashed line indicates the terminus position and the red line across the fjord indicates the ICESat-2 track along which surface elevation data is acquired. The date on the image shows the acquisition date for ICESat-2 data, which is around the same date of the presented satellite image. Upper left inset shows location of the glacier terminus in Greenland. Images are in polar stereographic projection (EPSG: 3413). (d)-(f) Surface elevation profiles extracted along ICESat-2 tracks in (a)-(c), after accounting for the local difference between the ellipsoid and the geoid. The horizontal axis shows the distance from the terminus (black dashed line in (a)-(c)). Solid and dashed lines represent the surface elevation data acquired from different dates. Note that for Kangerlussuaq on 14 Aug 2020 (dashed line in (e)), there is an increase in surface elevation at distance 1∼1.5 km from the terminus due to the presence of a large iceberg. (g)-(i) Black dots show the terminus position relative to 1 Sep 2021, 1 Jan 2020, and 1 Jan 2019 for Jakobshavn Isbræ, Kangerlussuaq Glacier, and Store Glacier, respectively. Here, the positive sign indicates terminus advance. Calving events are inferred from satellite images. The vertical solid and dashed lines mark the dates for ICESat-2 data presented in (d)-(f).

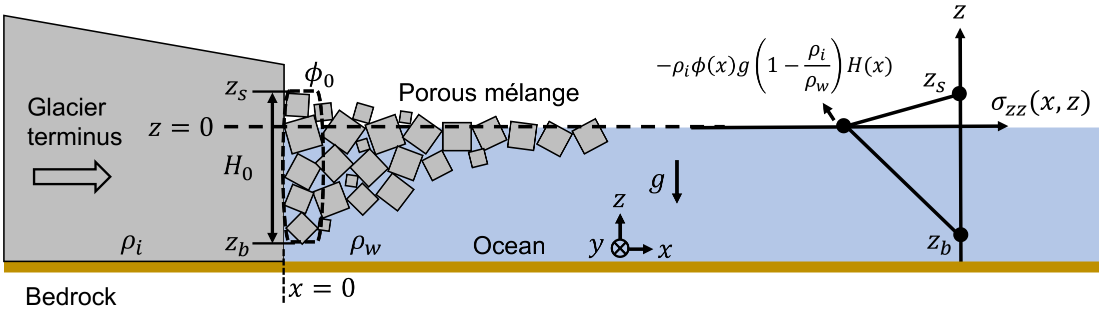

Figure 3: Schematic of the glacier–ocean–mélange system. Since mélange is a porous medium, the skeleton stress σ_{zz} vanishes at its bottom free surface [42, 43, 44].

1.3 A three-dimensional continuum model of ice mélange.

Remote sensing observations reveal a strong correlation between mélange thickness and calving dynamics. As a result, quantifying buttressing force of mélange in terms of its thickness is the first step to better representing ice-ocean interactions and developing process-based calving models. Building on the one-dimensional model of ice flow [41, 29], we derive a three-dimensional continuum model for ice mélange, and then validate it by discrete element modeling. Figure 3 shows a schematic of the glacier-ocean-mélange system. We use Cartesian coordinate system, with x starting from the terminus and in the direction along the fjord, y in the direction across the fjord, and z in the vertical direction with $z = 0$ at sea level. We begin by defining a number of variables that are required for describing the continuum models. First, we define the strain rate tensor as $\dot{\epsilon}_{ij} = \frac{1}{2}(\frac{\partial u_i}{\partial x_j} + \frac{\partial u_j}{\partial x_i})$, where u_i is the velocity component and x_i is the spatial coordinate. u, v, w denote the velocity in the x, y, z components, respectively. The Cauchy stress tensor $\sigma_{ij} = \sigma_{ji}$ partitions into deviatoric stress σ'_{ij} and the hydrostatic pressure p via $\sigma_{ij} = -p\delta_{ij} + \sigma'_{ij}$, where $p = -\frac{1}{3}\sigma_{kk}$ and δ_{ij} is the Kronecker delta. Here, compressive stresses have negative values. The trace of the deviatoric stress tensor is equal to zero, that is, $\sigma'_{xx} + \sigma'_{yy} + \sigma'_{zz} = 0$.

We make the following assumptions: (i) the fjord width is a constant; (ii) the mélange is in a three-dimensional state; (iii) the mélange packing density, thickness, viscosity, and strain rates are uniform across the width of the fjord and the across the depth of the mélange, but vary with the distance from terminus; (iv) a viscous constitutive relationship between the mélange deviatoric stress and the strain rate, that is, $\sigma'_{ij} = 2\eta\dot{\epsilon}_{ij}$, where η is the effective mélange viscosity. As the trace of the deviatoric stress tensor is equal to zero, the mélange flow is incompressible, that is, $\dot{\epsilon}_{xx} + \dot{\epsilon}_{yy} + \dot{\epsilon}_{zz} = 0$; (v) variations of horizontal velocities across the depth of the mélange are negligible, that is, $\frac{\partial w}{\partial x} \sim \frac{\partial w}{\partial y} \ll \frac{\partial u}{\partial z} \sim \frac{\partial v}{\partial z} \cong 0$, and therefore $\sigma'_{xz} = \sigma'_{yz} = 0$; and (vi) the bottom of the mélange is fully permeable and leaves the skeleton stress-free. Such assumption align with the fact that the effective stress always vanishes at the free surface of the solid skeleton in a porous medium [42, 43, 44].

Under steady flow conditions, the vertical force balance for ice mélange states that:

$$\frac{\partial \sigma_{zz}}{\partial z} = \rho_i \phi(x) g', \tag{1}$$

where ρ_i is the density of ice, $\phi(x)$ is the packing density of ice mélange that varies along the fjord direction, and g' is the effective acceleration due to gravity (depending on if the ice is above or below the waterline). Since the vertical stress in ice mélange equals zero at its top and bottom surface, we arrive at a final expression for vertical stress σ_{zz} (Fig. 3):

$$\sigma_{zz}(x,z) = \begin{cases} \rho_i \phi(x) g \left(z - (1-\frac{\rho_i}{\rho_w}) H(x) \right), \text{where } 0 < z < (1-\frac{\rho_i}{\rho_w})H(x), \\ (\rho_i - \rho_w)\phi(x) g \left(z + \frac{\rho_i}{\rho_w} H(x) \right), \text{where } -\frac{\rho_i}{\rho_w}H(x) < z < 0. \end{cases} \tag{2}$$

where ρ_w is the density of sea water, and $H(x)$ is the mélange thickness that varies along the fjord direction. The equation states that the vertical stress for mélange linearly decreases from zero at the top to $-\rho_i\phi(x)g(1-\frac{\rho_i}{\rho_w})H(x)$ at sea level, and then linearly increases to zero at the bottom (Fig. 3). With some algebraic steps we derive the mélange buttressing force per width on the terminus as follows (see SI for derivation details):

$$\frac{F}{W} = \left(\int_{z_b}^{z_s} -\sigma_{xx}(x,z)dz \right) |_{x=0} = \frac{1}{2}\rho_i(1-\frac{\rho_i}{\rho_w})g\phi_0 H_0^2 - 4H_0(\eta\frac{\partial u}{\partial x})|_{x=0} - 2H_0(\eta\frac{\partial v}{\partial y})|_{x=0}. \tag{3}$$

where z_b, z_s are at the bottom and surface of the mélange and ϕ_0, H_0 are the mélange packing density and thickness at the terminus, respectively.

When the mélange packing density approaches 1, Eqn. (3) converges to the expression of ice shelf buttressing [45]. It is well known that an unconfined ice shelf (i.e., ice tongue) provides zero buttressing as the glaciostatic pressure balances out the extensional stress [46]. The horizontal momentum balance equation (Eqn. 8 in SI) shows that without lateral confinements from fjord walls and assuming a uniform velocity field, ice mélange cannot thicken near the terminus, and thus also provides zero buttressing force. In reality, fjords always provide lateral confinements on the mélange. Equation (3) states that the mélange buttressing force has two components: (i) the glaciostatic pressure induced by mélange thickness ($\propto H_0^2$), and (ii) horizontal deviatoric stresses induced by velocity gradients ($\propto \frac{\partial u}{\partial x}, \frac{\partial v}{\partial y}$). Previous studies have shown that winter velocity fields are generally steady and highly uniform in space [29, 28], whereas summer velocity fields tend to be much more variable and can be uniform, compressional, or extensional [29]. For dense mélange confined within a straight fjord, the velocity gradient along the fjord is much larger than that across the fjord, that is, $\frac{\partial u}{\partial x} \gg \frac{\partial v}{\partial y}$. To characterize the relative magnitude of the horizontal deviatoric stress to the glaciostatic pressure, we substitute representative values for parameters in Eqn. (3) and obtain:

$$\frac{|4H_0(\eta\frac{\partial u}{\partial x})|_{x=0}|}{\frac{1}{2}\rho_i(1-\frac{\rho_i}{\rho_w})g\phi_0 H_0^2} \in [4.68\times10^{-14}, 5.46\times10^{-12}]\times\eta, \tag{4}$$

where we take $H_0 \in$ [75 m, 200 m] [25, 28], $\frac{\partial u}{\partial x} \in [\frac{2\text{ m/day}}{15\text{ km}}, \frac{25\text{ m/day}}{10\text{ km}}]$ [29], $\phi_0 \in$ [0.64, 1] [47, 48], $\rho_i \in$ [870 kg/m^3, 920 kg/m^3] [23], and $\rho_w \in$ [1020 kg/m^3, 1029 kg/m^3] [49]. As the mélange acts as a weak granular ice shelf [28], its effective viscosity should be much smaller than the glacier ice viscosity, $\eta \ll \eta_i = 10^{12} - 10^{15}$ Pa·s [50, 51]. Therefore, for mélange with lower viscosity, glaciostatic pressure dominates and the mélange buttressing force can be approximated as:

$$\frac{F}{W} = \frac{1}{2}\rho_i(1-\frac{\rho_i}{\rho_w})g\phi_0 H_0^2. \tag{5}$$

which states that the mélange buttressing force is solely controlled by the packing density and mélange thickness at the glacier terminus. The mélange modeled in the following section has a viscosity of 2×10^{10} Pa·s (see Section 1 in SI for details). For mélange with higher viscosity ($\eta > 10^{12}$ Pa·s), we will need to consider deviatoric stress effects.

Table 1: Modeling parameters for the three-dimensional discrete element model

Symbol	Value	Unit	Variable
L	3	km	Initial length of the ice mélange
H_{ini}	[30, 380] with a mean step size 15	m	Initial thickness of the ice mélange
N_p	[1634, 15264] with a mean step size 1238		Total number of icebergs in a simulation
W	1	km	Fjord width
V_{ter}	43.2	m/day	Terminus velocity
C_w	0.5		Dimensionless drag coefficient for icebergs in seawater
E	2.6	MPa	Iceberg elastic modulus
$a_{\min}$	17.7	m	Minimum side length of a cubic iceberg
$a_{\max}$	141.4	m	Maximum side length of a cubic iceberg
d_r	150	m	Spacing between bulges on the rugged wall
a_r	60	m	Side length of bulges on the rugged wall
h_r	20	m	Thickness of bulges on the rugged wall
Δt	0.1	s	Modeling time step
δt_{buoy}	5	s	Time step to update the buoyant force for icebergs
μ	0.3		Kinetic friction coefficient between the particle and the wall
μ_p	1.0		Kinetic friction coefficient between particles
β	0.7		Iceberg critical damping ratio
ν	0.3		Iceberg Poisson's Ratio
ρ_i	910	kg/m^3	Iceberg density
ρ_w	1028	kg/m^3	Seawater density

1.4 A three-dimensional discrete element model of ice mélange.

To validate the continuum prediction on the mélange buttressing force (Eqn. (5)), we develop a three-dimensional discrete element model on the mélange with a steadily advancing terminus. Icebergs are modelled as cubic particles with a power-law size distribution [52, 53]. In a series of simulations, we vary the prescribed mélange thickness to determine its influence on the time- and width-averaged buttressing force exerted by mélange on the advancing terminus. We present modeling results for a thin and thick layer of ice mélange in Fig. 4, with the initial thickness, H_{ini}, equal to 60 m and 378 m, respectively. At the initial state, the ice mélange has a uniform thickness with the right end open to the ocean. We push the left end of the mélange with an advancing terminus at 43.2 meters per day [27, 28] and record the temporal evolution of the buttressing force exerted on the terminus. To explore the effect of fjord frictional properties on the mélange buttressing force, we adopt two channel configurations that resemble fjords in Greenland. The straight channel configuration (Fig. 4(b)(d)(g)(i)) has a constant-width fjord. The rugged channel configuration (Fig. 4(c)(e)(h)(j)) has uniformly-spaced bulges on both sides [28]. A summary of the modeling parameters is given in Table 1.

We present modeling results after 16 days of terminus motion, when the mélange motion has approximately reached a steady state. The thin layer of mélange expands into a two-dimensional monolayer (Fig. 4(b)(c)). The mélange thickness at a specific position reflects the height of an individual iceberg, which varies in space. The thick layer of mélange collapses into a three-dimensional granular heap with a thickness gradient (Fig. 4(g)(h)). The mélange thickness decreases with the distance from terminus, and becomes a two-dimensional monolayer at the open end in the ocean. In the straight channel configuration, the mélange behaves like plug flow with a uniform velocity profile within the fjord (Fig. 4(d)(i)). In the rugged channel configuration, the mélange exhibits shear bands near fjord boundaries (Fig. 4(e)(j)), which has also been reported in previous studies [28, 29]. The mélange switches between the jammed and unjammed state, as evidenced by noticeable fluctuations in the velocity and the buttressing force (see SI videos). In both channel configurations, the mélange near the open end becomes loosely-packed and more fluidic. (See supplementary videos for the full temporal evolution of the mélange behaviors.)

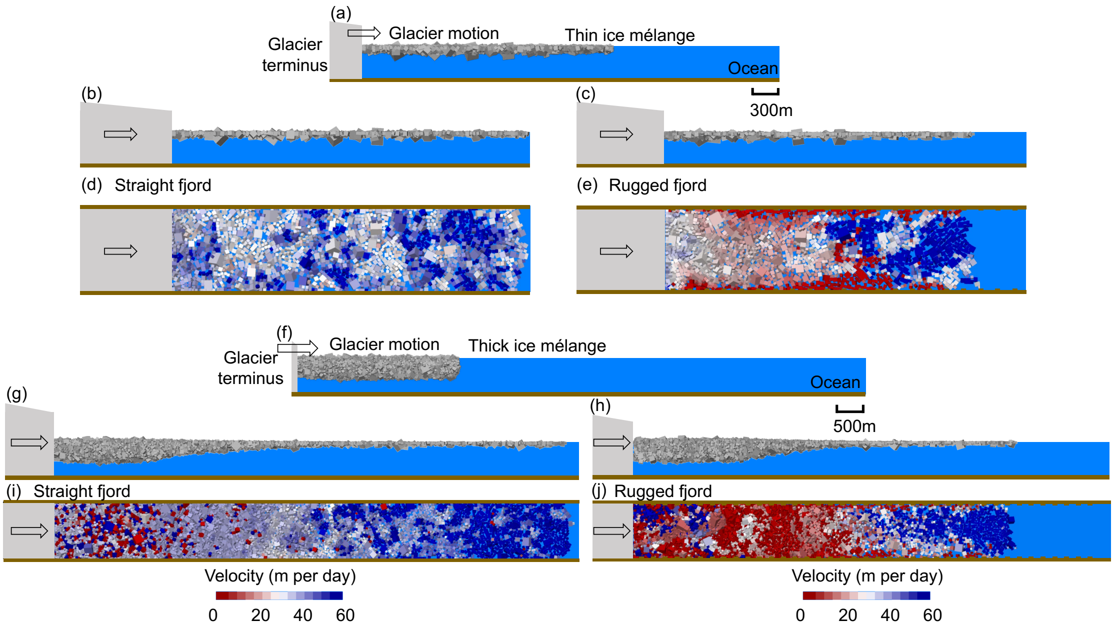

Figure 4: The three-dimensional discrete element model for mélange composed of cubic icebergs with a power-law size distribution. (a)-(e) For a thin mélange, (f)-(j) for a thick mélange. (a) A side view of the initial condition for the simulation with W = 1 km, L = 3 km, and H_{ini} = 60 m. The glacier terminus is shown as a grey block on the left. The ocean floor and fjord walls are plotted in brown. The glacier terminus starts to move at a constant velocity, V_{ter} = 43.2 m/day. (b)-(e) are snapshots for iceberg positions and velocities after 16 days into simulations with steady terminus advance and no calving. (b), (d) are the side and top view for a straight fjord wall configuration; (c), (e) are the side and top view for a rugged fjord wall configuration. Velocity of each iceberg element is indicated by filled colour in (d) and (e). (f) A side view of the initial condition for the simulation with W = 1 km, L = 3 km, and H_{ini} = 378 m. (g)-(j) follow captions of (b)-(e). See supplementary videos for the full temporal evolution of the mélange behaviors.

1.5 Mélange buttressing force increases with mélange thickness at glacier terminus.

We present the temporal evolution of the buttressing force for mélange with different initial thicknesses in straight and rugged channel configurations (Fig. 5(a)). For the same initial mélange thickness, the buttressing force is always larger in rugged channels (solid lines) than that in straight channels (dashed lines). The bulges in rugged channels increase the shear resistance from fjord walls, which results in larger buttressing forces exerted on the advancing terminus. This is also evidenced by the difference in the mélange length at steady state (Fig. 4). The mélange has a smaller length when confined within rugged channels compared with straight channels. By conservation of mass, the mélange has to be either thicker or more densely-packed (or both) within rugged channels, which leads to a larger buttressing force as predicted in Eqn. (5). The thickness and buttressing force of most mélange reach steady-state values after 5 days of simulation. Therefore, we take the time window 5$\sim$15 days to calculate their averaged steady state values.

To validate the continuum theory (Eqn. 5), we plot the steady state buttressing force and mélange thickness at the terminus for all simulations in Fig. 5(b). We calculate the averaged steady state buttressing force over the fjord width (F/W) with force fluctuations indicated as vertical error bars. We calculate the averaged mélange thickness within 200 m of the terminus (H_0), with thickness variations indicated as horizontal error bars. We also compute the packing density of the mélange within 200 m of the terminus (ϕ_0) and colour data markers by the magnitude of ϕ_0. For simulations that start with thin mélange and collapse into monolayers at the end, we plot both the minimum and maximum F/W values and connect them by gray lines. We compare the buttressing force predicted by the continuum equation (5) with simulations. The modeled buttressing force slightly deviates from the continuum prediction due to extra buttressing force induced by compressional flow that exists in simulations but has been neglected in Eqn. (5). However, the overall good match between modeling results and the continuum prediction shows that Eqn. (5) is robust and the glaciostatic pressure outweighs deviatoric stresses. A simple scaling analysis between glaciostatic pressure and fjord friction further shows that the mélange viscosity is around 2×10^{10} Pa·s (Section 1 in SI), which validates the assumption ($\eta < 10^{12}$ Pa·s) underlying Eqn. (5). For the four cases where the mélange collapses into thin monolayers at the end of the simulation (denoted as pentagram markers), the final buttressing forces can be predicted well by the previously developed theory for mélange of a uniform thickness [28] with the yield stress parameter, σ_0, fitted to be 0.12 kPa $\sim$ 0.16 kPa. The modeled buttressing forces in these cases are smaller than in the three-dimensional continuum (Eqn. (5); black lines in Figure 5), because the mélange only has a monolayer and violates the assumption of three-dimensional mélange with a constant packing density throughout its depth. Our modeling results confirm that, whether the fjord walls are straight (smooth) or rugged (rough), the thickness of the mélange at the terminus directly indicates its buttressing force. As the fjord friction increases, fjords are able to pile up thicker and denser mélange at the glacier terminus. The robustness of Eqn. (5) with different fjord properties is the key to interpreting field observations across Greenland glacier termini.

1.6 Calving dynamics associated with mélange thickness seasonality across 32 Greenland glacier termini in 2013-2022.

Our models reveal that the mélange buttressing force can be predicted solely from remote sensing observations of its thickness at glacier terminus (Eqn. (5)). However, further investigation is needed to address the question of how does the spatio-temporal variations in mélange thickness correlate with calving dynamics in Greenland. Recent studies covering the period from 2015

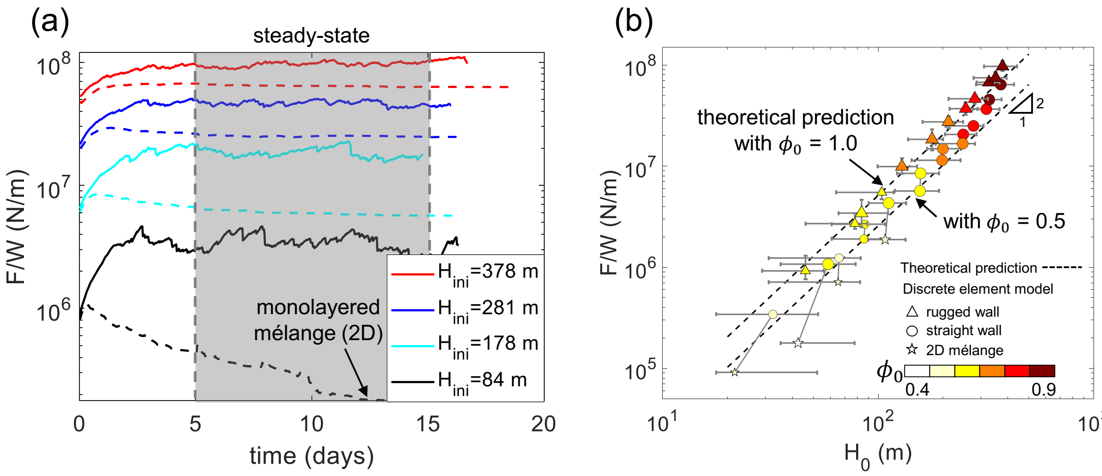

Figure 5: Comparison between discrete element model and continuum predictions of mélange buttressing force. (a) The temporal evolution of F/W during the terminus motion for straight (dashed lines) and rugged (solid lines) fjord walls. The red, blue, cyan and black colours correspond to mélange with initial thicknesses, H_{ini} = 378 m, 281 m, 178 m, 84 m, respectively. Simulations reach the steady state after 5 days, except for the thinnest mélange (H_{ini} = 84 m). (b) Steady state buttressing force, F/W, as a function of steady-state mélange thickness at the terminus, H_0. Circular markers indicate simulations with straight fjord walls, and triangular markers indicate simulations with rugged fjord walls. The smaller markers indicate simulations with smaller icebergs (half of the original size). F/W is obtained by averaging the total buttressing force on the terminus over the terminus width during simulation time 5 $\sim$ 15 days. The marker shows the averaged steady-state value of F/W, with a vertical error bar showing its fluctuation. H_0 is obtained by averaging the mélange thickness within 200 m of the terminus and over the terminus width. The marker shows the averaged steady-state value of H_0, with a horizontal error bar showing its variation over the terminus width brought by the iceberg size polydispersity. For simulations where the mélange collapse into monolayers at the end, we plot both the peak and minimal F/W values and connect them by gray lines. The minimal F/W values for monolayered, two-dimensional mélange are shown by pentagram markers. All markers are coloured by the mélange packing density at the terminus at steady state, ranging from 0.4 to 0.9. The dashed lines represent Eq. (5) with the mélange packing density at the terminus, ϕ_0 = 0.5 and 1.0, respectively.

to 2021 found that among 219 marine-terminating glaciers in Greenland, nearly 80% of them showed significant seasonal variations in terminus position, which retreat in summer and advance in winter [54]. We hypothesis that the seasonal terminus-position variability could be induced by a mélange thickness seasonality. To test this hypothesis, we collect available ArcticDEM strips at Jakobshavn Isbræ in the past decade, and compare DEM acquisition dates to a time series of the terminus position (Fig. 6(a)). Among the eight DEM strips, five of them (dashed lines) are acquired in summer when the terminus retreats, and three of them (solid lines) are acquired in winter when the terminus advances. From the corresponding mélange elevation profiles constructed the same way as in Fig. 1 (solid blue lines in Fig. 6(f)-(i)), we first confirm that they are not contaminated by large icebergs whose elevation values are above 30 m (Fig. 6(b)-(e)). The elevation profile successfully reflects the overall thickness variations within the mélange that piled up from small icebergs. We observe that the freeboard height of the mélange at the terminus ranges from $2.8 \sim 3.9$ m in summer and $19.2 \sim 26.8$ m in winter.

We then extend our study to 32 glacier termini, most of which (ID 1$\sim$25) are picked from previous studies with strong terminus-position seasonality [37, 38], and the rest (ID 26$\sim$32) have annual ice discharge larger than 5 Gt/yr [55]. The locations of the termini are marked on a Greenland velocity map in Fig. 7(a). Across mélange regions in front of the 32 glacier termini, we identify 60 ArcticDEM strips collected during terminus advance periods and 48 ArcticDEM strips collected during terminus retreat periods, from March to October in 2013–2022. Table. 1 in SI summarizes the observed minimum (or maximum) mélange thickness when terminus retreats (or advances) as $H_0^{\min}$ (or $H_0^{\max}$), with the corresponding DEM acquisition month shown in the bracket. We also present all observed mélange freeboard heights at the terminus (Z_0) in Fig. 7(b). A complete catalog of terminus position variations, DEM acquisition dates and mélange freeboard heights for 32 studied termini is summarized in SI. Assuming the mélange to be densely-packed with $\phi_0 = 0.9^{+0.1}_{-0.26}$, ice density in the plausible range of 910^{+10}_{-40} kg/m^3 and water density of 1028^{+1}_{-8} kg/m^3, we arrive at the mélange buttressing force per unit width (F/W) through Eqn. (5). For the studied glacier termini, the observed mélange thicknesses when terminus advances (85% in winter) range from 60^{+21}_{-23} m to 240^{+52}_{-69} m, with buttressing forces ranging from $1.7^{+1.3}_{-1.1} \times 10^6$ N/m to $2.7^{+1.1}_{-1.4} \times 10^7$ N/m. Previous force balance analysis of a calving iceberg revealed that for a terminus at floatation, mélange buttressing force of order $\sim 1.0 \times 10^7$ N/m is sufficient to inhibit calving by preventing iceberg rotation [24]. Finite element models suggested that mélange buttressing force of this magnitude can also inhibit calving by suppressing fracture propagation [25, 26, 34, 4, 33]. Most of our inferred buttressing forces during terminus advance are consistent with the proposed threshold. The observed mélange thicknesses when terminus retreats (90% in summer) range from 1^{+11}_{-1} m to 87^{+26}_{-29} m, with inferred buttressing forces ranging from $0.1^{+6.2}_{-0.1} \times 10^4$ N/m to $3.5^{+2.1}_{-2.1} \times 10^6$ N/m. Therefore in summer, mélange is generally too thin to inhibit calving.

2 Discussion

Previous research suggests that the presence of ice mélange can reduce iceberg calving by providing "backstress" to the terminus [23, 19, 27, 17, 24, 18, 28, 29, 26, 25, 22]. The mélange momentum balance along the fjord direction (Eqn. (8) in SI) reveals three competing forces: compressional/extensional flow from velocity gradients within the mélange (negligible if mélange viscosity is smaller than 10^{12} Pa·s), glaciostatic stress from mélange thickness, and shear stresses on fjords. Therefore, the full thickness profile of the mélange depends on fjord/mélange friction/cohesion properties, velocity gradients and viscosity of the mélange, and the mélange width/length. To quantify the mélange buttressing force, previous two-dimensional model assuming mélange of

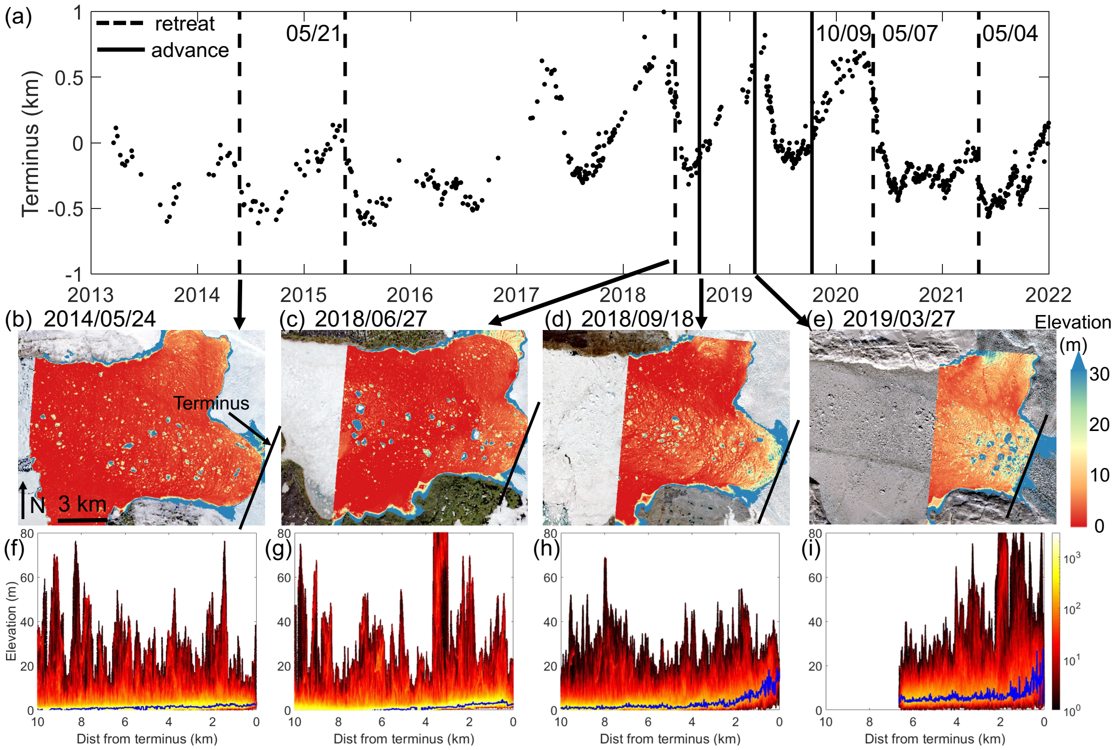

Figure 6: Seasonal variations in mélange thickness coincide with calving dynamics at Jakobshavn Isbræ. (a) Terminus position in 2013-2022 [39] where positive sign indicates the direction of advance. Eight vertical black lines mark the acquisition dates of available ArcticDEMs, four of which are prensented in (b)-(e), corresponding to 24 May 2014, 27 Jun 2018, 18 Sep 2018, and 27 Mar 2019, respectively. Solid black lines mark the dates with terminus advances, and dashed black lines mark the dates with terminus retreats. (b)-(e) The mélange elevation above mean sea level from ArcticDEM strips, overlain on satellite images acquired around the same date. Black line across the fjord indicates glacier front location. The images are in polar stereographic projection (EPSG: 3413). (f)-(i) Surface elevation profiles for the mélange displayed as density plots (8,649,023 $\sim$ 18,183,005 data points in total) constructed the same way as in Fig. 1. We observe thick mélange in winter when terminus advances, and thin mélange in summer when terminus retreats.

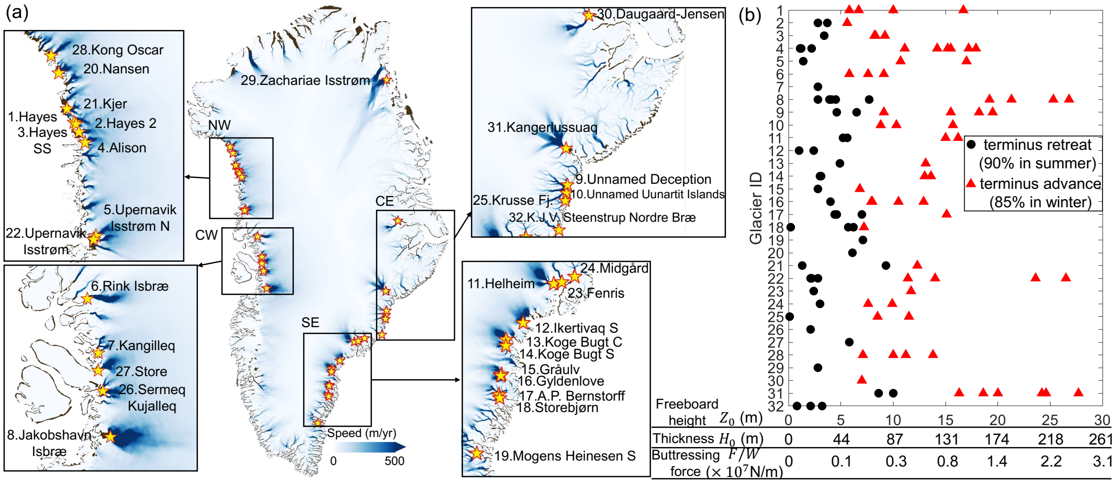

Figure 7: Seasonal changes of mélange thickness and buttressing forces across 32 Greenland glacier termini in 2013-2022. (a) Locations of the 32 studied glacier termini are shown as pendular markers on the background Greenland ice velocity map belonging to 1 Dec 2020 - 30 Nov 2021. We also present zoomed in views of the studied glacier termini in northwest (NW), central west (CW), southeast (SE), and central east (CE) regions of Greenland. (b) From 2013 to 2022, the observed mélange freeboard heights at the terminus (Z_0) from all available ArcticDEM (108 in total). Red triangular markers correspond to DEM acquired when terminus advances (85% in winter), and black circular markers correspond to DEM acquired when terminus retreats (90% in summer). The horizontal axis contains three variables: the mélange freeboard height directly retrieved from DEM (Z_0), the inferred mélange thickness from hydrostatic equilibrium (H_0), and the inferred mélange buttressing force from Eqn. (5) (F/W). Data used to calculate the buttressing forces and their uncertainties are listed in Table 1 in SI.

uniform thickness required approximations on these parameters [28]; in our three-dimensional model the mélange thickness at the terminus is the only parameter needed. As the length and thickness are coupled by stress balances within the granular material, the mélange thickness build-up at the terminus already encodes the aforementioned material and geometric properties. For instance, thicker mélange can be built up at the terminus with longer fjords, larger fjord friction, or increased mélange rigidity in winter. It is also worth noting that our discrete element model of ice mélange is the first to be composed of realistic cubic icebergs instead of spheres. The model can be used to further explore how the mélange thickness at the terminus evolves with ice-ocean interactions that influence calving dynamics, including ocean tides [14], ocean warming [40, 20, 21], and subglacial plumes [56, 13].

Our modeling results are consistent with observational data. Scanning through 108 ArcticDEM strips, we discover calving dynamics associated with mélange thickness seasonality across 32 Greenland glacier termini in 2013-2022. When termini advance in winter, the average value of all observed mélange thicknesses is 119^{+31}_{-37} m, with a corresponding buttressing force $6.5^{+3.4}_{-3.7} \times 10^6$ N/m. When termini retreat in summer, the average thickness is 34^{+17}_{-15} m, with a corresponding buttressing force of $5.2^{+5.9}_{-3.8} \times 10^5$ N/m. While we have observed strong evidence of correlations between mélange thickness and terminus seasonality, understanding their causality requires considerations of other environmental forcings. Previous research shows that seasonal terminus positions for some central west Greenland glaciers with small-magnitude calving events correlate stronger with glacial runoff than mélange presence or ocean thermal forcing [57]. On the other hand, researchers observe slowdown and thickening of Jakobshavn since 2016 and attribute it to concurrent cooling of ocean waters [58]. Analytical and numerical models imply that submarine melting can amplify calving by melt-undercutting [7, 59]. We note that if submarine melting causes the observed summer thinning of mélange, mélange's buttressing strength can be strongly tied to submarine melts. The impact of submarine melt on mélange strength can be significant due to the strong dependence of buttressing on mélange thickness inferred in our study.

We note that the hypothesis of summer-runoff induced calving, on its own, can not explain our observations of six advancing termini in summer: 1) Hayes Glacier SS in Jun 2018 with a mélange thickness $H_0 = 71^{+23}_{-25}$ m, 2) Alison Glacier in Jun 2017 with $H_0 = 124^{+32}_{-39}$ m, 3) Unnamed Deception in Jun 2016 with $H_0 = 135^{+34}_{-42}$ m, 4) Unnamed Uunartiti Islands in Aug 2018 with $H_0 = 90^{+26}_{-30}$ m, 5) Koge Bugt C in Jul 2015 with $H_0 = 114^{+30}_{-36}$ m, and 6) Kong Oscar Glacier in Jul 2014 with $H_0 = 98^{+27}_{-32}$ m. We attribute these summertime terminus advances to mélange buttressing from the presence of unusually thick mélange, the same as for Jakobshavn Isbræ in Jun 2016 [23]. If calving dynamics are controlled by mélange buttressing, then our analysis infers that the minimum buttressing force required to inhibit calving varies across termini from $1.1^{+0.9}_{-0.7} \times 10^6$ (Hayes Glacier 2) to $9.3^{+4.6}_{-5.2} \times 10^6$ N/m (Kangerlussuaq Glacier). Such variations in the buttressing threshold could be attributed to spatial variations in ice velocities, terminus geometry, bed topography, basal friction, bathymetry, oceanic and atmospheric forcings, etc. Our analysis offers a new framework to mechanistically study the effects of mélange buttressing and other ice-ocean interactions on calving.

In summary, our continuum and discrete element models offers a way to estimate the mélange buttressing force with a single measurement: freeboard height (or thickness) of the mélange at the terminus. Our field data analysis show that mélange thickness seasonality strongly correlates with calving dynamics across Greenland. As termini keep retreating inland, the emergence of longer fjords could retain more icebergs and potentially enhance mélange thickness (especially in winter), which could slow down the process of overall termini retreat, as has been observed at Steenstrup [40]. Given that mélange thickness dictates its buttressing force, the impacts of submarine melting and subglacial discharge on calving will be amplified by melting and thinning the mélange. On the other hand, cooler ocean and air temperature in winter enhances mélange rigidity [21], making it easier to pile up thick mélange at the terminus to provide buttressing. How warmer ocean and atmospheric influence the mélange strength is the subject of future work. Lastly, our models provide a simple way to incorporate mélange effects into large-scale numerical ice sheets models. Knowing the mélange thickness at the terminus, the mélange buttressing force can be calculated by Eqn. (5) and imposed as the boundary condition for ice sheet models. Our result indicates that climate change, manifested in lengthening summer seasons, can weaken the mélange buttressing effect, accelerating terminus recession and ice mass loss at tidewater glaciers in Greenland.

3 Methods

3.1 Terrestrial laser scanner data and uncertainty assessment.

ATLAS generated point clouds were gridded at 100 m × 100 m resolution to insure sufficient point densities per grid cell using the Point Cloud Data Abstraction Library (PDAL) [60] for DEM creation. The resulting DEMs contain a minimum, maximum, and average band where each point which falls into a 100 m × $\sqrt{2}$ radius contributes to a grid cell. Generally, five main sources of uncertainty exist when using terrestrial laser scanner (TLS) data. These sources being registration, atmospheric conditions, scanning geometry, instrument and hardware limitations, rasterization, and surface reflectance properties [61]. From our 2019-2020 registration scan we can conclude an average vertical accuracy of ± 0.10 m for each scan. Though this accuracy does vary with distance from the scanner [61].

3.2 ICESat-2 data and uncertainty assessment.

We use the ATL06 data set from ICESat-2 that provides geolocated, land-ice surface heights above the WGS 84 ellipsoid. The spatial resolution is 20 m and the temporal resolution is 91 days from 14 October 2018 to present. We compute the mélange surface elevation after accounting for the local difference between the ellipsoid and the geoid with tidal corrections [36]. There are very few ICESat-2 tracks passing through the fronts of termini in different seasons, because positions of termini vary seasonally but ICESat-2 tracks are generally fixed in space. We identify three ICESat-2 tracks for Jakobshavn Isbræ, Kangerlussuaq Glacier and Store Glacier, respectively, and use data from strong beams to compose the mélange elevation profile (Fig. 2). The averaged standard error in the reported elevation data ranges from 0.02 m∼0.52 m due to sampling error and first-photon bias correction from the land ice algorithm [62].

3.3 ArcticDEM data and uncertainty assessment.

From 2013 to 2022, we identified 341 ArcticDEM strips at 2-meter resolution that covered the mélange regions for the 32 studied termini. For each DEM strip, we investigated terminus position variations [39] during a two-month time window centering on the DEM acquisition date. If terminus kept advancing (or retreating) within the time window, then the DEM potentially represented mélange with strong (or weak) buttressing force. If terminus alternated between advancing and retreating within the time window, we discarded the corresponding DEM strip because the relationship between mélange and calving dynamics was ambiguous in this case. After filtering all DEM strips through this criterion, we identified 60 DEM strips during terminus advances, and 48 DEM strips during terminus retreats. For each glacier terminus, we digitized terminus positions using ArcticDEMs on the dates when the data was acquired. For mélange of length 15 km and width 4 km, there were approximately 15,000,000 data points available. For each data point in a DEM strip, we calculated its distance from terminus and the surface elevation value after accounting for the local difference between the ellipsoid and the geoid with the tidal correction [36]. After picking specific values for the number of horizontal and vertical bins, we displayed all data points in a density map where surface elevation was plotted as a function of distance from terminus (Fig. 3 in SI). For any specific distance from terminus, we find the elevation value that had the maximum number of data points (Fig. 2 in SI). We then connected these values along the distance from terminus as the representative mélange elevation profiles (solid blue lines in Fig. 6), $Z(x)$. We calculated the maximum mélange elevation within 200 m from the terminus as Z_0. The value Z_0 was further divided by $1 - \rho_i/\rho_w$ to obtain the mélange thickness, H_0, which was used for calculating the buttressing force, F/W, based on Eqn. (5).

To improve the vertical accuracy of DEM strips, we registered each DEM strip with the mosaic DEM [63], which has been registered to ICESat-2. For each glacier terminus, we selected line segments on neighboring rock (Fig. 5 – 36 in SI) and calculated averaged elevation offsets between individual DEM strips and the mosaic DEM along these line segments. After applying the elevation offset and subtracting the geoid from the ellipsoid with the tidal correction [36], we plotted DEM elevation values above mean sea level in a histogram with 0.25 m bin widths, making sure its peak (i.e. the most common elevation above mean sea level in the DEM) was larger or equal to sea level at the time when the DEM was acquired [53]. In summary, the elevation offsets applied to the 108 DEM strips were 0.38±2.23 m. With this protocol, the elevation accuracy of the DEM strip segment improved from 4 m [64] to 1.06 m [63, 65]. The accuracy from varying the number of bins of density maps ranged from 0.11∼0.27 m (Fig. 2 in SI). In Table. 1 in SI, we report the thickness uncertainty arising from ArcticDEM (±1.06 m), ice (910^{+10}_{-40} kg/m^3) and water (1028^{+1}_{-8} kg/m^3) densities. The uncertainties in ice and water densities, mélange packing density ($\phi_0 = 0.9^{+0.1}_{-0.26}$), and the mélange thickness fed into Eqn. (5) to obtain the uncertainty in the buttressing force, F/W.

3.4 The three-dimensional discrete element model for quasi-static flow of ice mélange.

We develop a three-dimensional discrete element model for ice mélange with a commercial software, PFC3D® [66]. We use the same Cartesian coordinate system as in Section. 1.3, with x starting from the terminus and in the direction along the fjord, y in the direction across the fjord, and z in the vertical direction with $z = 0$ at sea level. Iceberg interactions are simulated using a classical Hertzian model for elastic contact between disks with a Coulomb friction law and viscoelastic damping to maintain stability. The kinetic friction coefficient between the particle and the wall, $\mu = 0.3$, is adopted from [28]. The kinetic friction coefficient between particles is set to $\mu_p = 1.0$. The particles also experience small viscous drag force that is proportional to the iceberg velocity to represent hydrodynamic drag from seawater. To impose buoyant force on an individual iceberg, we need to identify its relative position to the sea water level, which is prescribed at $Z = 0$. As it is computational expensive to compute the indentation of a cubic particle into a plane, we instead use a surrogate sphere that has the same center positions and volume of the cubic particle for buoyancy calculations. Assuming the side length of the cubic particle is a, then the surrogate sphere has the radius, $r = (\frac{3a^3}{4\pi})^{1/3}$. We calculate the immersed volume of the surrogate sphere in the seawater and obtain the corresponding buoyant force on an individual cubic iceberg. As positions of icebergs are evolving during simulations, we update their buoyant forces on a regular basis, $\delta t_{\text{buoy}} = 5$ s. The mechanical timestep is chosen to be the same as in previous two-dimensional discrete element model [28] to maintain mechanical stability, $\Delta t = 0.1$ s.

We use cubic grains which can achieve a higher packing density, thus buttressing forces, than disk-shaped grains. We adopt the iceberg size distribution observed in the mélange of Jakobshavn Isbræ and Heiheim Glacier, which is approximated as a power-law distribution with an exponent of -2.0 [52, 53]. Taking the simulation of the thick mélange for instance (Fig. 4(f)), the side lengths of cubic icebergs are 35.4 m, 50 m, 70.7 m, 100 m, 141.4 m, and the corresponding numbers of particles are 8190, 2045, 510, 125, 30, respectively. In most simulations, the iceberg size always ranges from 35.4 m to 141.4 m, with the initial mélange thickness dictated by the total number of particles. To confirm that the modeling results are invariant to the particle size, we conduct six more simulations with smaller icebergs, whose sizes are half of original sizes and range from 17.7 m to 70.7 m (small markers in Fig. 5(b)).

To construct the initial mélange state, we divide the total number of particles into three equal batches. In each batch, iceberg sizes are randomly drawn from the distribution described above. We put a right boundary wall at distance L from the terminus on the left to prescribe the initial length of the mélange. The mélange is confined in y direction by two side walls representing fjords at a distance W. To explore influence of fjord friction properties on mélange behaviors, we have straight and rugged channel configurations. Both configurations have the same kinetic friction coefficient, μ, and rugged channels have cuboid bulges of dimension $a_r \times a_r \times h_r$ that are uniformly spaced at d_r in x and z directions. We deposit icebergs in each batch from the same height and then they settle under gravity and buoyancy. Following pouring, the entire array of cubic particles is permitted to settle until static equilibrium is achieved, as shown in Fig. 4(a)(f). We then delete the right boundary wall so that the mélange has an open end in the ocean. We move the terminus on the left at a constant velocity, $V_{\text{ter}} = 43.2$ m/day [27, 28]. To confirm that the averaged steady-state buttressing force is invariant to the terminus velocity, we conducted simulations with mélange thickness 280 m, terminus velocity at 21.6 m/day, 43.2 m/day, and 86.4 m/day, for both straight fjords and rugged fjords configurations (Fig. 4 in SI). The results show that the averaged buttressing force is mostly invariant to the terminus velocity in both fjord configurations. Taking the force fluctuations into account, the maximum buttressing force difference among the chosen velocities is 4% and 8% for straight and rugged fjords, respectively. In rugged fjords, faster terminus motion leads to larger force fluctuations due to larger velocity gradient during stick-slip/jam-unjam cycles. We adopt the terminus velocity of 43.2 m/day for simulations in the paper for the sake of computational efficiency.

3.5 Estimating modeling mélange thickness and packing density at glacier termini and uncertainty assessment.

As icebergs have a power-law size distribution, the thickness of mélange is a spatial variable in horizontal directions (x and y). We compute the mélange thickness at each particle position within a sampling cylinder of radius 80 m and capped by icebergs at the top and the bottom of the mélange. We then take an average of thickness values for icebergs within 200 m from the terminus and display it as a marker in Fig. 5(b), with the horizontal error bar denoting the minimum and maximum thickness values. Therefore, the reported uncertainty of the mélange thickness comes from polydispersity and varies within 90 m $\sim$ 140 m. In comparison, the mélange thickness uncertainty from doubling the sampling cylinder radius is below 15 m, and therefore is neglected here.

To compute the packing density of the mélange, we focus on its dependency along the fjord direction and set an interval size (dx) of 67 m. We compute the averaged mélange thickness at each interval with the aforementioned method and obtain $H(x)$. At each interval, we divide the total volume of icebergs by the total volume of the mélange ($H(x) \times W \times dx$) and obtain the packing density, $\phi(x)$. We then take an average of the first three intervals to output the packing density at the terminus, ϕ_0. The uncertainty in ϕ_0 by doubling the interval size is below 0.05 and therefore we only report the first decimal place for ϕ_0 in Fig. 5(b).

4 Data availability

Landsat images were downloaded through the USGS EarthExplorer (https://earthexplorer.usgs.gov/). Sentinel-1/2 data provided by European Space Agency and were downloaded through the USGS EarthExplorer and Alaska Satellite Facility (https://www.asf.alaska.edu/). TLS data for Helheim Glacier are available upon reasonable request. ICESat-2 laser altimetry tracks are available through the OpenAltimetry portal at https://openaltimetry.org/data/icesat2/ with download services provided by the National Snow and Ice Data Center. ArcticDEM digital elevation models [64] are available from the University of Minnesota Polar Geospatial Center (PGC): https://www.pgc.umn.edu/data/arcticdem/. Ice surface velocity and BedMachine Greenland are freely available at the National Snow and Ice Data Center (NSIDC) at https://nsidc.org/data/nsidc-0725/versions/5 and https://nsidc.org/data/idbmg4/versions/5, respectively. The time series of Greenland terminus positions is available from [39] at https://zenodo.org/records/10095674. Elevation offsets applied on the 108 ArcticDEM strips are included in the supplementary excel file.

5 Code availability

The codes used for the three-dimensional discrete element model are available from the corresponding author upon reasonable request. PFC3D® [66] is a software from Itasca Consulting Group, Inc. through a commercial license.

References

[1] Aschwanden, A. *et al.* Contribution of the greenland ice sheet to sea level over the next millennium. *Science advances* **5**, eaav9396 (2019).

[2] Hofer, S. *et al.* Greater greenland ice sheet contribution to global sea level rise in cmip6. *Nature communications* **11**, 6289 (2020).

[3] Choi, Y., Morlighem, M., Rignot, E. & Wood, M. Ice dynamics will remain a primary driver of greenland ice sheet mass loss over the next century. *Communications Earth & Environment* **2**, 26 (2021).

[4] Todd, J., Christoffersen, P., Zwinger, T., Råback, P. & Benn, D. I. Sensitivity of a calving glacier to ice–ocean interactions under climate change: new insights from a 3-d full-stokes model. *The Cryosphere* **13**, 1681–1694 (2019).

[5] Alley, R. *et al.* Iceberg calving: Regimes and transitions. *Annual Review of Earth and Planetary Sciences* **51**, 189–215 (2023).

[6] Goelzer, H. *et al.* The future sea-level contribution of the greenland ice sheet: a multi-model ensemble study of ismip6. *The Cryosphere* **14**, 3071–3096 (2020).

[7] Benn, D. I. *et al.* Melt-under-cutting and buoyancy-driven calving from tidewater glaciers: new insights from discrete element and continuum model simulations. *Journal of Glaciology* **63**, 691–702 (2017).

[8] Levermann, A. *et al.* Kinematic first-order calving law implies potential for abrupt ice-shelf retreat. *The Cryosphere* **6**, 273–286 (2012).

[9] Reeh, N., Thomsen, H. H., Higgins, A. K. & Weidick, A. Sea ice and the stability of north and northeast greenland floating glaciers. *Annals of Glaciology* **33**, 474–480 (2001).

[10] Joughin, I. *et al.* Continued evolution of jakobshavn isbrae following its rapid speedup. *Journal of Geophysical Research: Earth Surface* **113** (2008).

[11] Amundson, J. M. *et al.* Glacier, fjord, and seismic response to recent large calving events, jakobshavn isbræ, greenland. *Geophysical Research Letters* **35** (2008).

[12] Sundal, A. *et al.* Controls on short-term variations in greenland glacier dynamics. *Journal of Glaciology* **59**, 883–892 (2013).

[13] Amundson, J. M. *et al.* Formation, flow and break-up of ephemeral ice mélange at leconte glacier and bay, alaska. *Journal of Glaciology* **66**, 577–590 (2020).

[14] Cassotto, R. K., Burton, J. C., Amundson, J. M., Fahnestock, M. A. & Truffer, M. Granular decoherence precedes ice mélange failure and glacier calving at jakobshavn isbræ. *Nature Geoscience* **14**, 417–422 (2021).

[15] Wehrlé, A., Lüthi, M. P. & Vieli, A. The control of short-term ice mélange weakening episodes on calving activity at major greenland outlet glaciers. *The Cryosphere* **17**, 309–326 (2023).

[16] Howat, I. M., Box, J. E., Ahn, Y., Herrington, A. & McFADDEN, E. M. Seasonal variability in the dynamics of marine-terminating outlet glaciers in greenland. *Journal of Glaciology* **56**, 601–613 (2010).

[17] Foga, S., Stearns, L. A. & Van der Veen, C. Application of satellite remote sensing techniques to quantify terminus and ice mélange behavior at helheim glacier, east greenland. *Marine Technology Society Journal* **48**, 81–91 (2014).

[18] Cassotto, R., Fahnestock, M., Amundson, J. M., Truffer, M. & Joughin, I. Seasonal and interannual variations in ice melange and its impact on terminus stability, jakobshavn isbræ, greenland. *Journal of Glaciology* **61**, 76–88 (2015).

[19] Moon, T., Joughin, I. & Smith, B. Seasonal to multiyear variability of glacier surface velocity, terminus position, and sea ice/ice mélange in northwest greenland. *Journal of Geophysical Research: Earth Surface* **120**, 818–833 (2015).

[20] Bevan, S. L., Luckman, A. J., Benn, D. I., Cowton, T. & Todd, J. Impact of warming shelf waters on ice mélange and terminus retreat at a large se greenland glacier. *The Cryosphere* **13**, 2303–2315 (2019).

[21] Joughin, I., Shean, D. E., Smith, B. E. & Floricioiu, D. A decade of variability on jakobshavn isbræ: ocean temperatures pace speed through influence on mélange rigidity. *The Cryosphere* **14**, 211–227 (2020).

[22] Walter, J. I. *et al.* Oceanic mechanical forcing of a marine-terminating greenland glacier. *Annals of Glaciology* **53**, 181–192 (2012).

[23] Xie, S., Dixon, T. H., Holland, D. M., Voytenko, D. & Vaňková, I. Rapid iceberg calving following removal of tightly packed pro-glacial mélange. *Nature communications* **10**, 3250 (2019).

[24] Amundson, J. M. *et al.* Ice mélange dynamics and implications for terminus stability, jakobshavn isbræ, greenland. *Journal of Geophysical Research: Earth Surface* **115** (2010).

[25] Todd, J. & Christoffersen, P. Are seasonal calving dynamics forced by buttressing from ice mélange or undercutting by melting? outcomes from full-stokes simulations of store glacier, west greenland. *The Cryosphere* **8**, 2353–2365 (2014).

[26] Krug, J., Durand, G., Gagliardini, O. & Weiss, J. Modelling the impact of submarine frontal melting and ice mélange on glacier dynamics. *The Cryosphere* **9**, 989–1003 (2015).

[27] Robel, A. A. Thinning sea ice weakens buttressing force of iceberg mélange and promotes calving. *Nature Communications* **8**, 14596 (2017).

[28] Burton, J. C., Amundson, J. M., Cassotto, R., Kuo, C.-C. & Dennin, M. Quantifying flow and stress in ice mélange, the world's largest granular material. *Proceedings of the National Academy of Sciences* **115**, 5105–5110 (2018).

[29] Amundson, J. M. & Burton, J. Quasi-static granular flow of ice mélange. *Journal of Geophysical Research: Earth Surface* **123**, 2243–2257 (2018).

[30] Nick, F. M., Van der Veen, C. J., Vieli, A. & Benn, D. I. A physically based calving model applied to marine outlet glaciers and implications for the glacier dynamics. *Journal of Glaciology* **56**, 781–794 (2010).

[31] Vieli, A. & Nick, F. M. Understanding and modelling rapid dynamic changes of tidewater outlet glaciers: issues and implications. *Surveys in geophysics* **32**, 437–458 (2011).

[32] Cook, S. *et al.* Modelling environmental influences on calving at helheim glacier in eastern greenland. *The Cryosphere* **8**, 827–841 (2014).

[33] Barnett, J., Holmes, F. A. & Kirchner, N. Modelled dynamic retreat of kangerlussuaq glacier, east greenland, strongly influenced by the consecutive absence of an ice mélange in kangerlussuaq fjord. *Journal of Glaciology* **69**, 433–444 (2023).

[34] Todd, J. *et al.* A full-stokes 3-d calving model applied to a large greenlandic glacier. *Journal of Geophysical Research: Earth Surface* **123**, 410–432 (2018).

[35] Peters, I. R. *et al.* Dynamic jamming of iceberg-choked fjords. *Geophysical Research Letters* **42**, 1122–1129 (2015).

[36] Howard, S. L. & Padman, L. Gr1kmtm: Greenland 1 kilometer tide model (2021).

[37] Moon, T. *et al.* Distinct patterns of seasonal greenland glacier velocity. *Geophysical research letters* **41**, 7209–7216 (2014).

[38] Vijay, S. *et al.* Resolving seasonal ice velocity of 45 greenlandic glaciers with very high temporal details. *Geophysical Research Letters* **46**, 1485–1495 (2019).

[39] Zhang, E., Catania, G. & Trugman, D. T. Autoterm: an automated pipeline for glacier terminus extraction using machine learning and a "big data" repository of greenland glacier termini. *The Cryosphere* **17**, 3485–3503 (2023).

[40] Chudley, T. R., Howat, I. M., King, M. D. & Negrete, A. Atlantic water intrusion triggers rapid retreat and regime change at previously stable greenland glacier. *Nature Communications* **14**, 2151 (2023).

[41] Van der Veen, C. J. *Fundamentals of glacier dynamics* (CRC press, 2013).

[42] MacMinn, C. W., Dufresne, E. R. & Wettlaufer, J. S. Fluid-driven deformation of a soft granular material. *Physical Review X* **5**, 011020 (2015).

[43] Auton, L. C. & MacMinn, C. W. Large poroelasto-plastic deformations due to radially outward fluid injection. *Journal of the Mechanics and Physics of Solids* **132**, 103690 (2019).

[44] Meng, Y., Li, W. & Juanes, R. Crossover from viscous fingering to fracturing in cohesive wet granular media: a photoporomechanics study. *Soft Matter* **19**, 7136–7148 (2023).

[45] Rignot, E. Evidence for rapid retreat and mass loss of thwaites glacier, west antarctica. *Journal of Glaciology* **47**, 213–222 (2001).

[46] Gudmundsson, G. Ice-shelf buttressing and the stability of marine ice sheets. *The Cryosphere* **7**, 647–655 (2013).

[47] Liu, L., Li, Z., Jiao, Y. & Li, S. Maximally dense random packings of cubes and cuboids via a novel inverse packing method. *Soft matter* **13**, 748–757 (2017).

[48] Li, S., Zhao, J., Lu, P. & Xie, Y. Maximum packing densities of basic 3d objects. *Chinese Science Bulletin* **55**, 114–119 (2010).

[49] Nayar, K. G., Sharqawy, M. H., Banchik, L. D. *et al.* Thermophysical properties of seawater: A review and new correlations that include pressure dependence. *Desalination* **390**, 1–24 (2016).

[50] Fowler, A. C. Glaciers and ice sheets. In Díaz, J. I. (ed.) *The Mathematics of Models for Climatology and Environment*, 301–336 (Springer Berlin Heidelberg, Berlin, Heidelberg, 1997).

[51] Bassis, J. N. & Kachuck, S. B. Beyond the stokes approximation: shallow visco-elastic ice-sheet models. *Journal of Glaciology* 1–12 (2023).

[52] Enderlin, E. M., Hamilton, G. S., Straneo, F. & Sutherland, D. A. Iceberg meltwater fluxes dominate the freshwater budget in greenland's iceberg-congested glacial fjords. *Geophysical Research Letters* **43**, 11–287 (2016).

[53] Shiggins, C. J., Lea, J. M. & Brough, S. Automated arcticdem iceberg detection tool: insights into area and volume distributions, and their potential application to satellite imagery and modelling of glacier–iceberg–ocean systems. *The Cryosphere* **17**, 15–32 (2023).

[54] Black, T. E. & Joughin, I. Weekly to monthly terminus variability of greenland's marine-terminating outlet glaciers. *The Cryosphere* **17**, 1–13 (2023).

[55] Mouginot, J. *et al.* Forty-six years of greenland ice sheet mass balance from 1972 to 2018. *Proceedings of the national academy of sciences* **116**, 9239–9244 (2019).

[56] Melton, S. M. *et al.* Meltwater drainage and iceberg calving observed in high-spatiotemporal resolution at helheim glacier, greenland. *Journal of Glaciology* **68**, 812–828 (2022).

[57] Fried, M. *et al.* Reconciling drivers of seasonal terminus advance and retreat at 13 central west greenland tidewater glaciers. *Journal of Geophysical Research: Earth Surface* **123**, 1590–1607 (2018).

[58] Khazendar, A. *et al.* Interruption of two decades of jakobshavn isbrae acceleration and thinning as regional ocean cools. *Nature Geoscience* **12**, 277–283 (2019).

[59] Slater, D., Benn, D., Cowton, T., Bassis, J. & Todd, J. Calving multiplier effect controlled by melt undercut geometry. *Journal of Geophysical Research: Earth Surface* **126**, e2021JF006191 (2021).

[60] Butler, H., Chambers, B., Hartzell, P. & Glennie, C. PDAL: An open source library for the processing and analysis of point clouds. *Computers and Geosciences* **148**, 104680 (2021). URL `https://doi.org/10.1016/j.cageo.2020.104680`.

[61] Voordendag, A. *et al.* Uncertainty assessment of a permanent long-range terrestrial laser scanning system for the quantification of snow dynamics on Hintereisferner (Austria). *Frontiers in Earth Science* **11** (2023). URL `https://www.frontiersin.org/articles/10.3389/feart.2023.1085416/full`.

[62] Smith, B. *et al.* the ICESat-2 Science Team: ATLAS/ICESat-2 L3A Land Ice Height, Version 5, NASA National Snow and Ice Data Center Distributed Active Archive Center, Boulder, Colorado, USA [dataset] (2021).

[63] Porter, C. *et al.* ArcticDEM - Mosaics, Version 4.1 (2023). URL `https://doi.org/10.7910/DVN/3VDC4W`.

[64] Porter, C. *et al.* ArcticDEM - Strips, Version 4.1 (2022). URL `https://doi.org/10.7910/DVN/C98DVS`.

[65] Howat, I., Negrete, A. & Smith., B. Measures greenland ice mapping project (grimp) digital elevation model from geoeye and worldview imagery, version 2 (2022). URL `https://nsidc.org/data/NSIDC-0715/versions/2`.

[66] Itasca Consulting Group, Inc. *PFC — Particle Flow Code, Ver. 7.0.* Minneapolis: Itasca (2021).

6 Acknowledgements

C.-Y.L. acknowledges funding from NSF's Office of Polar Programs through OPP-2235051.

7 Author contributions

Y.M. led the project and the preparation of the manuscript. Y.M. and C.-Y.L. conceived the study. R.C. provided guidance on data processing from remote observations. M.S. and L.S. supplied and interpreted terrestrial TLS data. C.-Y.L., J.B., and K.N. helped with the model development. All authors contributed to the scientific interpretation of the results, and the writing of the manuscript.

8 Competing interests

The authors declare no competing interests.

9 Additional information

Supplementary information The online version contains supplementary material available at xxxx.

Correspondence and requests for materials should be addressed to Yue Meng at olivmeng@stanford.edu.

Supplementary Files

This is a list of supplementary files associated with this preprint. Click to download.

- Terminioffsettide.xlsx
- melangeSI.pdf
- SI1ThinMeldemo.mp4
- SI2ThickMeldemo.mp4